

# Explainable deep-learning detection of microplastic fibers via polarization-resolved holographic microscopy

JAN APPEL,<sup>1</sup> MARIKA VALENTINO,<sup>2</sup> LISA MICCIO,<sup>2,\*</sup> VITTORIO BIANCO,<sup>2</sup> RAFFAELLA MOSSOTTI,<sup>3</sup> GIULIA DALLA FONTANA,<sup>3</sup> MIROSLAV JEŽEK,<sup>1</sup> PIETRO FERRARO,<sup>2</sup> JAROMÍR BĚHAL<sup>1,\*</sup>

<sup>1</sup>*Department of Optics, Palacký University, 17. listopadu 12, 77900, Olomouc, Czechia*

<sup>2</sup>*Istituto di Scienze Applicate e Sistemi Intelligenti “Eduardo Caianiello” (ISASI-CNR), via Campi Flegrei 34, 80078, Pozzuoli, Napoli, Italy*

<sup>3</sup>*STIIMA-CNR Institute of Intelligent Industrial Technologies and Systems for Advanced Manufacturing, National Research Council of Italy, 13900 Biella, Italy;*

*\*jaromir.behal@upol.cz, lisa.miccio@cnr.it*

**Abstract:** Reliable identification of microplastic fibers is crucial for environmental monitoring but remains analytically challenging. We report an explainable deep-learning framework for classifying microplastic and natural microfibers using polarization-resolved digital holographic microscopy. From multiplexed holograms, the complex Jones matrix of each fiber was reconstructed to extract polarization eigen-parameters describing optical anisotropy. Statistical descriptors of nine polarization characteristics formed a 72-dimensional feature vector for a total of 296 fibers spanning six material classes, including polyamide 6, polyethylene terephthalate, polyamide 6.6, polypropylene, cotton and wool. The designed fully connected deep neural network achieved an accuracy of 96.7 % on the validation data, surpassing that of common machine-learning classifiers. Explainable artificial intelligence analysis with Shapley additive explanations identified eigenvalue-ratio quantities as dominant predictors, revealing the physical basis for classification. An additional reduced-feature model with the preserved architecture exploiting only these most significant eigenvalue-based characteristics retained high accuracy (93.3 %), thereby confirming their dominant role while still outperforming common machine-learning classifiers. These results establish polarization-based features as distinctive optical fingerprints and demonstrate the first explainable deep-learning approach for automated microplastic fiber identification.

## 1. Introduction

Plastics have become pervasive in modern society, widely used in packaging, automotive components, construction materials, electronics, and textiles. However, their resistance to degradation and extensive post-consumer accumulation have raised serious environmental concerns. Nowadays, microscopic polymer particles known as microplastics (in the size range of 0.001–5 mm) are recognized as emerging pollutants [1]. These particles, whether intentionally manufactured at microscopic scale (primary microplastics) or formed through fragmentation of larger plastics (secondary microplastics), have been detected across various environmental compartments, including marine and freshwater systems, soils, and even the atmosphere. Their potential to enter food webs and accumulate in living organisms has prompted increasing attention to their potential environmental and health impacts [2, 3].

The global textile industry shift toward synthetic fibers contributes to a marked increase in microfiber pollution. Indeed, a significant subset of microplastics originates from synthetic micron-sized fiber fragments (MFFs) shed from textiles, accounting for 35 % of the primary microplastics in the oceans [4, 5]. The physical characteristics of synthetic MFFs, including small diameter, elongated shape, and low density, allow a substantial fraction to bypass conventional

wastewater treatment. As a result, they can be discharged into rivers, lakes, and marine environments in significant quantities, which makes synthetic textile fibers a major source of microplastic water contaminants [6, 7]. These MFFs, typically composed of polyester, polyamide, or polypropylene, are released into the environment during common processes such as laundering, wear, and mechanical abrasion. Unlike natural fibers, synthetic microfibers are almost non-biodegradable and may retain chemical additives, dyes, or finishing agents, enhancing their persistence and potential toxicity in aquatic environments. Therefore, the identification and accurate classification of MFFs are crucial for understanding why microplastics have become such pervasive pollutants. Such insights are critical for advancing mitigation strategies and identifying weaknesses in the textile production lifecycle, including washing, processing, recycling, and disposal, that contribute to environmental contamination [8].

Currently, no standardized method exists for microplastic identification and characterization. Instead, a range of analytical approaches are employed with their pros and cons, including visual identification, sieving, staining, gravimetric, spectroscopic, thermal analyses, and other methods [9–11]. Visual methods are simple but operator-dependent and size-limited, although the specific staining with Nile red may categorize particles according to sample surface polarity [12]. Scanning electronic microscopy coupled with energy dispersive X-ray spectroscopy is non-destructive and provide morphological and elemental analysis but the procedure is costly and requires cumbersome sample preparation, limiting number of samples that can be handled [13]. Methods based on analysis of the burning properties and solvent resistance, such as pyrolysis coupled with gas chromatography and mass spectrometry or thermal desorption gas chromatography–mass spectrometry, provide chemical signatures but are destructive thus making the sample unavailable for subsequent analysis [14]. Vibrational spectroscopies, such as attenuated total reflectance Fourier transform infrared (ATR-FTIR) [15], focal plane array (FPA)-based micro FTIR [16, 17], Raman [18], micro-Raman [19], and micro-FT-NIR [20], are widely used nondestructive polymer-specific identification techniques, though their require careful pretreatment because their performance may be degraded by interference with pigments, surroundings, organic matter, water, fluorescence signals, or low sample concentrations [13, 14].

Among label-free non-destructive optical methods, digital holography enables volume detection and characterization of microplastics in aqueous environments due to its numerical refocusing capability [21, 22]. Quantitative phase imaging based on digital holography further provides the optical path difference, which is related to the morphology and refractive index of a sample. The technique was also combined with machine learning approaches [23, 24] to overcome the limited specificity of digital holography for classification enhancement. Alternative promising strategies exploit polarization-sensitive techniques such as polarized light microscopy [25, 26] and polarization-resolved digital holography [27, 28], including Jones phase microscopy [29, 30], which enable material-specific eigen-polarization-based analysis of MFFs [31, 32].

Distinguishing between different types of MFFs represents a typical multiclass classification task. Machine learning tools [33–35] are nowadays applied to such problems, especially with high-dimensional data where intuitive rules for class assignment are rarely feasible [36–39]. On the other hand, the nature of the data also guides the choice of learning paradigm, which in turn affects both methodology and interpretation of results. Especially, when samples are accompanied by explicit labels, supervised learning is typically employed, whereas in situations where only a portion of the data are labeled, semi-supervised learning can be utilized. On the contrary, when labels are absent altogether, unsupervised learning is applied; this does not result in explicit classification but rather in discovering natural groupings based on feature similarity. Moreover, it is also essential to distinguish between hard and soft classification, depending on the nature of the output decision. In hard classification, the model unambiguously assigns a sample to a single class. In contrast, soft classification provides probability distributions across classes, thus offering information about the degree of uncertainty in predictions made by the employed

model.

Machine learning methods consequently differ in both their underlying principles and applicability to specific data types, respectively [40, 41]. The K-nearest neighbors is one of the most frequently applied algorithms, which classifies each sample according to the majority class among its K-nearest neighbors in the feature space. The naive Bayes classifier employs Bayes theorem under the assumption of feature independence, estimating the class to which a sample most likely belongs. Decision trees operate by sequentially partitioning data according to rules based on individual attribute values, while their more robust extension, random forests, aggregate the outcomes of multiple trees for improved performance with sufficient robustness against overfitting. The support vector machine method seeks to find the optimal separating hyperplane with the maximal margin between classes, and it is effective for classification with limited datasets. Logistic regression is often used for binary classification, modeling class membership probability via the logistic function. Boosting methods such as gradient boosting iteratively build an ensemble of weak classifiers, each correcting the errors of its predecessors, making them effective for use with limited datasets. Finally, artificial neural networks, especially when implemented in deep learning architectures, utilize layers of interconnected neurons to model complex, non-linear relationships [42, 43]. Each of these techniques exhibits specific strengths and limitations regarding interpretability, classification accuracy, robustness to noise, and computational requirements.

In particular, deep neural networks have been implemented, providing enhanced microplastic classification capabilities. Convolutional neural network (CNN)-based models were successfully used to distinguish microplastics from organic materials and to classify microplastics using Raman spectra [44, 45]. Furthermore, various CNN models [46, 47] have been applied to classify images of large marine microplastics [48]. Finally, deep learning has been combined with digital holography, to overcome its limited specificity, yielding improved classification performance by exploiting raw interference patterns [49] as well as reconstructed amplitude and phase masks through image fusion techniques [50].

In this work, we present non-destructive label-free MFF classification using a deep neural network with unprecedented accuracy. In particular, we analyze four types of common synthetic MFFs, including polyamide 6 (PA 6), polyethylene terephthalate (PET), polyamide 6.6 (PA6.6), polypropylene (PP), and two types of common natural MFFs (cotton and wool) under polarization-resolved digital holographic microscope. The retrieved eigen-parameters are calculated from the measured polarization Jones matrix of the sample and related to the MFF geometry. Set of such quantities compose features used for the subsequent classification pipeline. We show that these features enable efficient classification with the deep neural network, achieving 97% accuracy, thus outperforming common machine learning classifiers. Furthermore, we provide explainability analysis using SHAP framework to identify the polarization and statistical features most dominant for the classification performance.

## 2. Measurements and feature extraction

This section describes setup used for polarization-sensitive holographic imaging as well as Jones matrix reconstruction, and extraction and meaning of MFF polarization characteristics determining features considered for subsequent classification pipeline.

Simplified sketch of the realized digital holographic microscope based on Mach-Zehnder interferometer is shown in Fig. 1(a). The initial spatially filtered, collimated, and polarized laser beam (Sapphire SF, wavelength 532 nm) is split and directed into three independent optical paths, i.e., a signal arm, a horizontally polarized reference arm, and a vertically polarized reference arm, respectively. The studied sample present in the signal arm is illuminated by diagonally (or antidiagonally) linearly polarized beam. The sample is imaged by a microscope objective MO1 (5 $\times$ /0.12) onto a camera (UI 1550SEC-HQ, 2.8  $\mu$ m square pixels) with lateral magnification

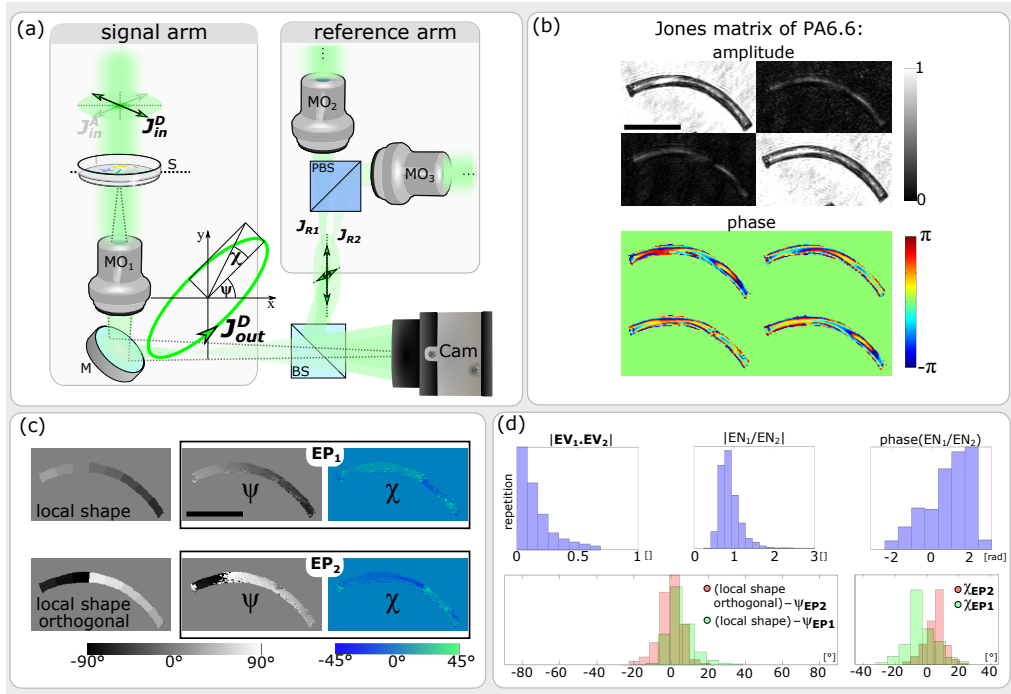


Fig. 1. (a) Simplified sketch of experimental configuration. (b) Example of retrieved Jones matrix for PA6.6 MF. (c) Local shape map and map orthogonal to the local shape compared to parameters of eigenpolarizations  $EP_1$  and  $EP_2$ , respectively. (d) Histograms of the derived polarization characteristic. Black scale bars in (b) and (c) represent  $100 \mu\text{m}$  lengths.

6.6. The mutually slightly tilted horizontally and vertically polarized reference beams  $J_{R1}$  and  $J_{R2}$  are combined via a polarizing beam splitter PBS and further injected into the signal arm via a beam splitter BS. All three mutually coherent beams interfere and create a multiplexed interference pattern recorded by the camera; hence a single-shot polarization state reconstruction is feasible. The microscope objectives MO<sub>2</sub> and MO<sub>3</sub> inserted in both reference arms reduce phase curvatures present in the reconstructed phase profiles.

Architecture of the holographic microscope allows reconstruction of complex amplitudes corresponding to horizontal and vertical polarization-state components, which are obtained via spectral filtering of the multiplexed interference pattern. Consequently, the polarization-state distribution across the observed field of view is reconstructed. Hence, for known polarization of the sample-illumination beam  $J_{in}^D$  the polarization-state distribution  $J_{out}^D$  in the detector plane is obtained. Similarly, for known initial polarization  $J_{in}^A$  the corresponding  $J_{out}^A$  is obtained. Assuming the  $J_{in}^D$  and  $J_{in}^A$  are orthogonally polarized the  $2 \times 2$  complex-amplitude Jones matrix, describing the polarization-response of the sample, can be calculated directly Fig. 1(b) [31].

Once the Jones matrix of the sample is retrieved its properties based on eigen-analysis can be evaluated. In Jones-matrix formalism it is often convenient to extract eigenvectors (EVs) and their associated eigenvalues (ENs) to better understand polarization properties of the sample. The EVs correspond to polarization modes that propagate throughout samples unaltered and are therefore described by the orientation angle  $\psi$  and the ellipticity angle  $\chi$ ; hence, the EVs are also referred to as eigenpolarizations (EPs). Each of the EVs is modulated in both amplitude and phase by its corresponding EN. Thus, the magnitude of the ENs' ratio indicates the degree

of anisotropic absorption, while the phase of this ratio reveals the relative phase delay between the two EVs [51]. Furthermore, the inner product of the EVs provides a measure of polarization homogeneity of the sample [52].

Initially, for each MFF a binary mask was calculated, which served as a reference for orientation-dependent polarization properties. For this purpose, the binary mask was further separated into several disjunct sub-binary masks whose main axis approximates the tangent of the MFF centre. We call such approximation a local shape Fig. 1(c). As can be noticed, the conjunction of all the sub-binary masks consequently creates the original binary mask. Moreover, the orientation perpendicular to this local shape indicates the orthogonal direction relative to the MFF axis. Indeed, a clear similarity between the local shape direction and the orientation angle  $\psi$  of  $EP_1$  ( $\psi_{EP1}$ ) in Fig. 1(c) justifies the use of the local shape map as a reference for  $\psi_{EP1}$ . Similarly, the direction orthogonal to the local shape serves as a reference for  $\psi_{EP2}$ , i.e., the orientation angle of  $EP_2$ . Calculations of EP orientations thus show that  $EP_1$  aligns with the MFF's principal axis, while  $EP_2$  tends to be approximately perpendicular Fig. 1(c).

For each analyzed MFF we calculated several polarization-based quantities. To avoid the influence of low-intensity pixels, all the calculations were accomplished only in areas of amplitude higher than 35 % of the average background amplitude. The considered quantities include the magnitude of the EVs inner product ( $|EV_1 \cdot EV_2|$ ), and the modulus, phase, real part, and imaginary part of the ENs ratio (i.e., ( $|EN_1/EN_2|$ ),  $\text{phase}(EN_1/EN_2)$ ,  $\text{Re}(EN_1/EN_2)$ ,  $\text{Im}(EN_1/EN_2)$ ), as well as the ellipticity angles  $\chi$  of  $EP_1$  and  $EP_2$  (i.e.,  $\chi_{EP1}$  and  $\chi_{EP2}$ ). Moreover, the polarization ellipse main axis orientation angles  $\psi$  of  $EP_1$  and  $EP_2$  (i.e.,  $\psi_{EP1}$  and  $\psi_{EP2}$ ) were also calculated and related to the MFF geometry via the local shape and the orientation perpendicular to the local shape, respectively. All these nine quantities will be referred to as polarization characteristics throughout the following text.

As noted above, it is obvious that each of the polarization characteristics calculated in a pixel-wise manner belong to numerous pixels inside the MFF camera image, hence each polarization characteristic provides its own statistics. Indeed, example histograms of the polarization characteristics calculated for PA6.6 MFF are present in Fig. 1(d). Thus, we further calculated several statistical parameters of such polarization characteristics, including mean value, median, mode, mean absolute deviation, median absolute deviation, standard deviation, skewness, and kurtosis.

To sum up, we calculated 8 statistical parameters for 9 polarization characteristics, creating a unique set of 72 numbers for each MFF, which we call features throughout the following text. In total, we analyzed 296 MFFs, prepared according to previously developed protocols [31], including 47 MFFs of PA6, 51 of PET, 46 of PP, 47 of PA6.6, 47 of cotton, and 58 of wool. Therefore, the input data used for the subsequent classification comprised of 296 measured MFFs belonging to six distinct classes and each analyzed MFF consisted of 72 features and a discrete label representing its class.

### 3. Neural network architecture

The following section details each step of the classification pipeline, including data preparation and normalization, data partitioning into training and validation sets, neural network design, and model accuracy evaluation.

The process of neural network training typically requires the division of the available dataset into at least two subsets: a training set and a validation set. In this study, the dataset of MFFs was chosen such that 80 % of the MFFs were allocated to the training set and 20 % to the validation set. This approach ensures development of a robust model with reliable generalization performance. Moreover, normalization of both input and output data is crucial for stable and efficient neural network learning. It transforms values to a common scale, such as mapping to [0,1] or applying zero mean and unit variance (Z-transformation). Importantly, the same procedure must also be

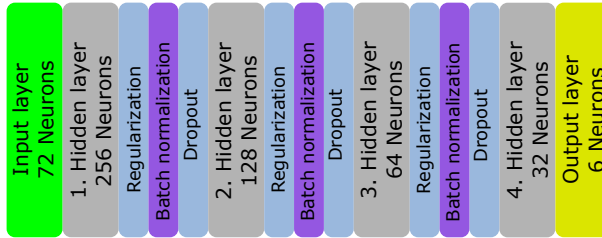


Fig. 2. The implemented neural network with input layer (green) with dimensions corresponding to the number of features. Four hidden layers (grey) with a progressively decreasing number of neurons. All hidden layers in the network employ regularization techniques, specifically: batch normalization, dropout and additional regularization methods, see text for details.

applied to validation data to ensure comparability of results and proper model performance on unseen data. In our case, we used Z-transformation. To address the classification task a fully connected (dense) neural network architecture was selected, which is a well-suited approach for modeling complex, non-linear relationships in such data. The use of fully connected network is justified by the tabular nature of the input data, where each MFF is represented by a fixed-length feature vector without inherent spatial or sequential structure.

The training process was conducted in a supervised learning regime, utilizing labeled data to optimize the network parameters. To account for class imbalance in the dataset, class weights were incorporated during training. The implemented neural network can be divided into three parts, see Fig. 2. A first input layer corresponds to the vector with 72 elements. Second part is composed of four hidden layers, each designed to progressively extract higher-level representations. Layers contain a progressively decreasing number of neurons: 256, 128, 64, and 32, respectively. This funnel-shaped architecture provides efficient abstract feature extraction. At the same time, the gradual reduction in the number of neurons leads to less computational effort. Finally, the output layer provides the final probabilities for each of the six MFF classes. Total number of trainable parameters is 63 thousands.

The first layer and all hidden layers have a rectified linear unit (ReLU) activation function. The last layer has a Softmax activation function due to its probabilistic interpretation suitable for multi-class classification [53]. To reduce overfitting and enhance generalization, architecture employed regularization techniques such as batch normalization and dropout layers [54] with relatively high dropout rates in first hidden layer (0.8) and gradually decreasing through the second hidden layer (0.4) to the third hidden layer (0.2). These layers also contain  $L_1$  and  $L_2$  regularizations. Their specific use ( $L_1$ ,  $L_2$ , or both) and values vary depending on the layer and its part (kernel, bias, and activity regularizer). The last hidden layer does not contain any regularization technique. Training was performed using the Adam optimizer [55] (initial learning rate 0.001) with categorical cross-entropy loss, and performance was monitored via categorical accuracy. The model was trained for up to 1500 epochs with a batch size of 50. A detailed layer-by-layer description of the architecture, including all regularization parameters, training callbacks, and the class weighting strategy, is provided in [56].

#### 4. Classification performance

To assess the performance of the trained model in detail, a confusion matrix approach is employed. For comparative evaluation, the confusion matrix was computed on the entire dataset, including the training samples, as it is sometimes considered to evaluate the classification performance with low number of samples, see Fig. 3(b). However, since assessing model accuracy on a dataset that

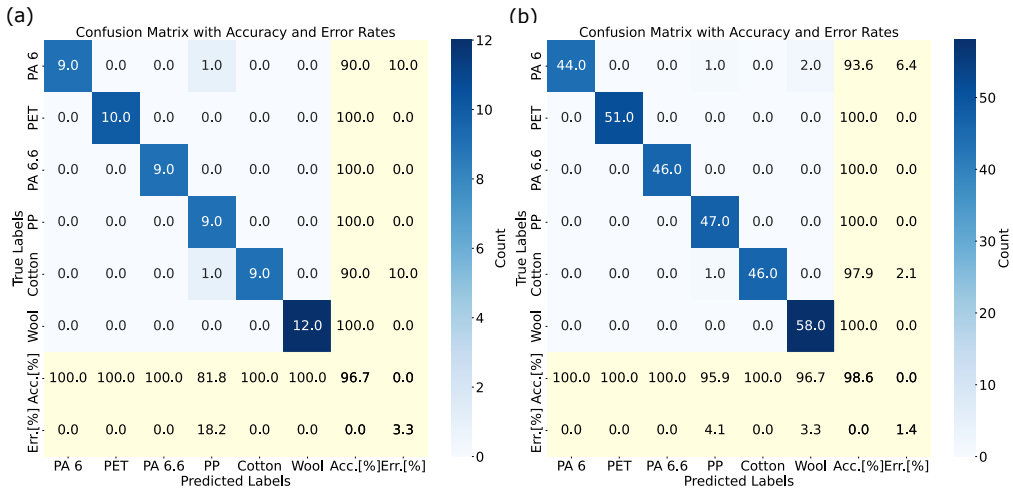


Fig. 3. Confusion matrix of the model trained on labeled data. (a) Evaluation on the validation data (60 labeled MFFs). (b) Evaluation on the complete dataset of training and validation data (296 labeled MFFs).

includes training data may provide an overly optimistic estimate of generalization performance, we also provide the confusion matrix for the validation data only, see Fig. 3(a). MFF classes in Fig. 3 are labeled as PA 6, PET, PA6.6, PP, cotton, and wool.

The confusion matrix in Fig. 3(a) summarizes the classification performance of the current model on the validation dataset consisting of 60 labeled MFFs. It provides a detailed breakdown of true versus predicted labels, including class-wise accuracy and error rates. Specifically, only two misclassifications appear among the MFF classes, both being false negatives for PP. In these cases, the model misclassified MFFs from PA 6 and cotton as PP. The diagonal values correspond to the number of true positives, which allows quantification of model accuracy. This accuracy is calculated by dividing their sum by the total number of predictions, yielding 96.7 % for our model, an unprecedented value in the field.

The confusion matrix in Fig. 3(b) summarizes the classification performance of the current model on the dataset containing all 296 labeled MFFs, i.e., the complete dataset including MFFs used for training. Across these 296 predictions, only four misclassifications occurred. Since the dataset contains complete data from the previous evaluation, two of these errors origin from the previous validation dataset—false positives for PA 6 and cotton, both misclassified as PP. In addition, two false negatives arise from the training data for PA 6: one misclassified as PP and the other as wool. The overall model accuracy on this dataset reaches 98.6 %.

Although the obtained results are very promising, the comparison with standard algorithms is required to rank quality of the proposed method. Therefore, other machine learning algorithms, including Gaussian naive Bayes, random forest, support vector machine, K-nearest neighbors, gradient boosting, and logistic regression, were systematically implemented in addition to the primary classification framework. Moreover, beyond algorithm selection, it is useful to assess multiple metrics for quick yet effective evaluation of classifier performance. While the confusion matrix enables detailed error analysis, metrics such as accuracy (returns the fraction of correctly classified samples), precision (ratio  $t_p/(t_p + f_p)$ , where  $t_p$  is the number of true positives and  $f_p$  the number of false positives), recall (ratio  $t_p/(t_p + f_n)$ , where  $f_n$  is the number of false negatives), and F1 score (2·precision·recall/(precision+recall)), which represents harmonic mean of precision and recall) offer a simplified assessment. Hence, for each technique, the attained metrics were evaluated specifically on the validation dataset, ensuring that the reported results objectively

reflect generalization performance and are not biased by the training process. The achieved results are summarized in Table 1, showing that the performance of these classifiers is inferior to the developed deep neural network, even when they are combined with a feature-selection preprocessing method based on mutual information [57, 58].

Table 1. Comparison of different classifiers. Values are reported as without feature selection / with feature selection.

Classifier	Accuracy	Precision	Recall	F1 score
Gaussian naive Bayes	0.80 / 0.82	0.81 / 0.83	0.80 / 0.82	0.80 / 0.82
random forest	0.83 / 0.85	0.84 / 0.86	0.83 / 0.85	0.83 / 0.85
K-nearest neighbors	0.87 / 0.90	0.88 / 0.91	0.86 / 0.90	0.86 / 0.89
support vector machine	0.88 / 0.90	0.88 / 0.91	0.88 / 0.90	0.88 / 0.90
gradient boosting	0.88 / 0.88	0.87 / 0.87	0.87 / 0.87	0.87 / 0.87
logistic regression	0.90 / 0.92	0.90 / 0.92	0.90 / 0.92	0.90 / 0.92
deep neural network (the main result of our work)	0.97	0.97	0.97	0.97

## 5. Explainability

We employ Shapley additive explanations (SHAP) to analyze the contribution of polarization-derived features used in the classification of MFFs. SHAP provides a principled, game-theoretic framework that decomposes each model prediction into additive contributions from individual input features relative to a baseline prediction [59–61]. To obtain a global measure of relevance, we report SHAP feature importance (SHAP-FI) values, defined as the average absolute SHAP values across all validation data points. A SHAP-FI value quantifies how strongly a particular feature, on average, shifts the model output in its natural prediction scale away from the baseline. This allows us to directly compare the relative influence of polarization characteristics and their statistical parameters on classification performance, thereby identifying which aspects of the polarization response carry the greatest predictive power for distinguishing between different MFFs.

Nevertheless, SHAP-FI values are not unique if the features are correlated or redundant, even for repeatedly retrained models with the same parameters [60, 62, 63]. For this reason, we performed an analysis of SHAP-FI values for twenty-eight trained models with the same architecture, accuracy, and confusion matrix. The calculated SHAP-FI values of each model were normalized with respect to their sum over the validation data. Mean values and standard deviations of the SHAP-FI values are shown in Fig. 4(a). The most significant polarization characteristic is the absolute value of the ENs ratio, i.e.  $|EN_1/EN_2|$ , with the sum of mean SHAP-FI values across all eight statistical parameters equal to 0.203, which can be compared to the overall sum of all SHAP-FI values of 1. Among them, the median absolute deviation (0.046) and the median (0.037) are simultaneously the highest of all 72 SHAP-FI values. In addition, Fig. 4(b) shows the sums of SHAP-FI values for the current polarization characteristics across all eight statistical parameters; ordered by their significance the sums reach as follows: 0.203 for  $|EN_1/EN_2|$ , 0.140 for  $\text{Im}(EN_1/EN_2)$ , 0.127 for  $\text{phase}(EN_1/EN_2)$ , 0.124 for  $\text{Re}(EN_1/EN_2)$ , 0.099 for  $|EV_1 \cdot EV_2|$ , 0.094 for  $\chi_{EP2}$ , 0.081 for  $\chi_{EP1}$ , 0.070 for  $\psi_{EP1\text{-sh.}}$ , and 0.062 for  $\psi_{EP2\text{-sh.orth.}}$ . It is worth noting that the first four most significant polarization characteristics

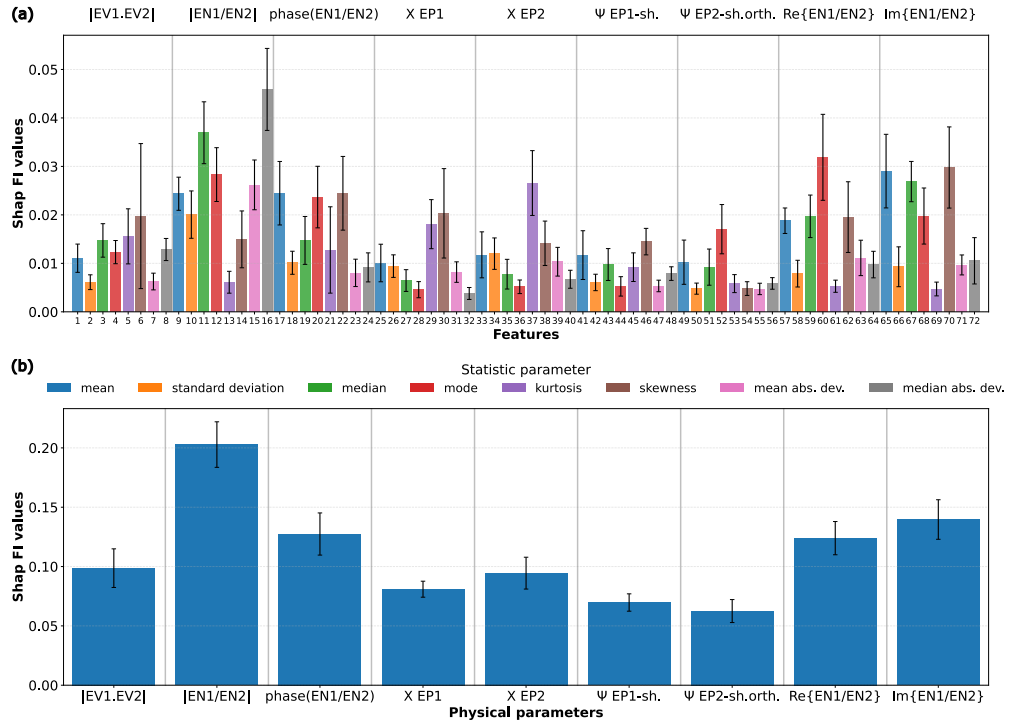


Fig. 4. SHAP-FI values of nine polarization characteristics and their eight corresponding statistical parameters, yielding 72 SHAP-FI values.  $|EV_1 \cdot EV_2|$  - magnitude of the EVs inner product;  $|EN_1/EN_2|$ ,  $\text{phase}(EN_1/EN_2)$ ,  $\text{Re}\{EN_1/EN_2\}$ ,  $\text{Im}\{EN_1/EN_2\}$  - modulus, phase, real part, and imaginary part of the ENs ratio;  $\chi_{EP1}$ ,  $\chi_{EP2}$  - ellipticity angles of  $EP_1$  and  $EP_2$ ;  $\psi_{EP1\text{-sh.}}$  - orientation of  $EP_1$  relative to the local shape;  $\psi_{EP2\text{-sh.orth.}}$  - orientation of  $EP_2$  relative to the direction perpendicular to the local shape.

are based on ENs only (sum 0.594) and not on EVs and EPs (sum 0.406). To be complete, the difference between the SHAP-FI values for statistical parameters (summed across polarization characteristics) is less pronounced than between the polarization characteristics (summed across statistical parameters), which were already discussed.

In the previous paragraphs, we analyzed SHAP-FI values without distinguishing individual material classes. For a deeper understanding, we provide a class-wise SHAP-FI value analysis. For clarity, we visualized the sum of SHAP-FI values of statistical parameters for individual polarization characteristics (see Fig. 5). It turned out that the ratio  $|EN_1/EN_2|$  is particularly significant for synthetic fibers. For natural fibers, the parameter  $\chi_{EP2}$  is the most significant for cotton and the parameter  $\text{Im}\{EN_1/EN_2\}$  is the most significant for wool, respectively.

Above findings enable to correlate SHAP-FI analysis with most significant material features of MFFs. Birefringence of MFFs originates from preferential alignment of molecular structures along the fiber, which leads to anisotropic polarizability and, consequently, to a refractive index difference parallel and perpendicular to the fiber. In particular, the intrinsic anisotropy of natural fibers appears due to the ordered arrangement of structural proteins or polysaccharides, i.e., keratin in the case of wool and crystalline cellulose in the case of cotton [64]. Importantly, the significance of class-wise SHAP-FI values for EP ellipticities ( $\chi_{EP1}$ ,  $\chi_{EP2}$ ) of cotton compared to other classes (Fig. 5) is the consequence of its twisted ribbon-like geometry, which arises due to the natural twisting of the cellulose-rich cell wall as it dries [65]. Such a complex structure

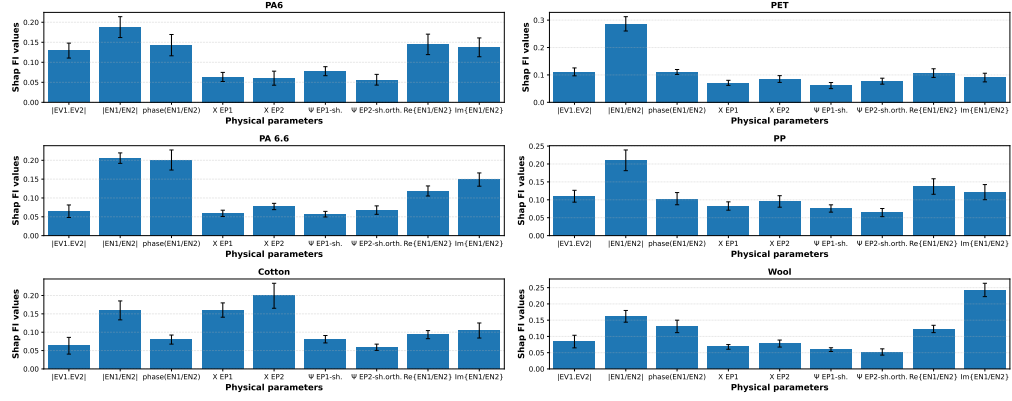


Fig. 5. Class-wise SHAP-FI values of nine polarization characteristics. The most significant polarization characteristic for synthetic fibers is the absolute value of the EN ratio, i.e.  $|EN_1/EN_2|$ . For natural fibers,  $X EP_2$  appears to be the most important indicator for cotton and  $Im(EN_1/EN_2)$  for wool.

determines the spatial variation of cellulose microfibrils along the local shape of MFF, thus broadening the distributions of  $X EP_1$  and  $X EP_2$  compared to the remaining material classes [31].

On the other hand, optical birefringence in polymer textile fibers originates mainly from the orientation of polymer chains, whose alignment is determined during the drawing process [66]. In particular, PET exhibits the highest value of the so-called virtual birefringence among the considered synthetic materials, exceeding 0.22 [67,68], which represents the theoretical maximum of birefringence achieved within ideally oriented material domains. This finding is consistent with our experimental observations that the relative absorption  $|EN_1/EN_2|$  is the most significant for PET among the remaining material classes [31], as a higher value of birefringence induces higher Fresnel losses compared to materials with an overall comparable mean value of refractive index but lower birefringence [69]. Indeed, the high importance of  $|EN_1/EN_2|$  is also confirmed via the class-wise SHAP-FI values of PET (Fig. 5), where it is relatively highest among all material classes, i.e. the SHAP-FI value of  $|EN_1/EN_2|$  of PET is 2.6 times higher than the second most important SHAP-FI value of PET, i.e.,  $phase(EN_1/EN_2)$ . In addition, a substantially high importance of  $|EN_1/EN_2|$  is also apparent for PP via the analysis of SHAP-FI values (Fig. 5).

Finally, both the overall and the class-wise SHAP-FI analysis identifies the EN-based features as the most important, as can be noticed in Fig. 4 and Fig. 5, respectively. To confirm the significance of  $|EN_1/EN_2|$  and  $phase(EN_1/EN_2)$  we selected all the relevant features (marked as 9-24 in Fig. 4) and created an additional neural-network based model without any changes to the previous architecture. The model thus enables classification using these 16 features related to ENs. Indeed, the final classification accuracy evaluated on validation dataset reached 93.3 %. This means that although the accuracy decreases by approximately 3.4 % compared to the previous model, it still outperforms the classification performance of any common classifier exploiting all 72 features or even when applying feature selection (Table 1). The proposed SHAP-FI analysis thus identified the most significant features based on ENs which allow efficient MFF classification.

## 6. Conclusions

In this manuscript, we have proposed a deep-neural network-based approach for the classification of MFFs. Initially, a polarization-sensitive digital holographic microscope was used to measure polarization characteristics of MFFs, which were extracted from the reconstructed Jones matrix,

including EPs defined by their orientation ( $\psi$ ) and ellipticity ( $\chi$ ) angles, and associated ENs describing amplitude and phase modulation. From these, nine polarization characteristics were derived, describing polarization homogeneity, modulation, ellipticity, and EP orientations related to the local fiber geometry. For each polarization characteristic, eight statistical parameters (mean, median, mode, mean absolute deviation, median absolute deviation, standard deviation, skewness, and kurtosis) were computed across all relevant pixels, yielding 72 features per MFF. In total, 296 MFFs from six material classes (PA6, PET, PP, PA6.6, cotton, and wool) were analyzed to form the input dataset for subsequent classification.

A classification method using a fully connected neural network was implemented to classify MFF types from the fixed-length feature vectors. The architecture comprised of an input layer with 72 elements, followed by four hidden layers with progressively decreasing sizes to extract increasingly abstract representations. Batch normalization and dropout were incorporated to reduce overfitting, and class weights were used to address dataset imbalance. The output layer generated probabilities for six classes. The model was trained using the Adam optimizer and categorical cross-entropy loss, with performance monitored via categorical accuracy. The proposed neural network classifier achieved high accuracy in distinguishing the considered MFF types. The accuracy on the validation dataset reached 96.7 %, while on the complete dataset it achieved 98.6 % accuracy.

Comparative evaluation against other machine learning methods, including Gaussian naive Bayes, random forest, support vector machine, K-nearest neighbors, gradient boosting, and logistic regression, confirmed the superior performance of the deep neural network, as reflected by consistently higher accuracy, precision, recall, and F1 score on the validation dataset. In particular, logistic regression performed best among the conventional methods, achieving 92 % classification accuracy, while the accuracy of the remaining methods ranged from 82 % to 90 %. The proposed deep neural network based approach thus improves the classification accuracy of at least 5 % compared to the standard classification approaches.

Furthermore, we quantified significance of the used polarization-derived features via SHAP-FI values. As a result, the most significant polarization characteristic is the absolute value of ENs ratio, i.e. ( $|EN_1/EN_2|$ ), with its statistical parameters—particularly the median and median absolute deviation—emerging as the strongest contributors among all features. Overall, the EN-based characteristics dominate the classification process, collectively surpassing the contributions of EV- and EP-based features.

Moreover, additional class-wise SHAP-FI analysis predicted the significant influence of EN based features, with exception of cotton, where ellipticity  $\chi_{EP2}$  proved to be the most important. The significance of ENs was confirmed via additional neural-network based classification model with the preserved architecture, while exploiting features relevant just to polarization characteristics  $|EN_1/EN_2|$  and phase( $EN_1/EN_2$ ). The final classification accuracy reached 93.3 %, thus still outperforming the classification performance of any above-noted machine-learning classifiers (see Table 1).

The achieved results show that polarization-derived features contain significant information for classifying MFFs. When combined with deep learning, these features enable highly accurate and interpretable classification, demonstrating the potential of polarization-sensitive digital holography as an effective tool for microplastic detection and analysis.

## Funding

J.B. acknowledges project of the Czech Science Foundation (GAČR), project No. 25-17712I. J.A. acknowledges projects IGA\_PrF\_2025\_005 and IGA\_PrF\_2026\_003 of Palacký University Olomouc. This work was partially supported by project ROMEO-smaRt Online Multisensory systEm for microplastic quantificatiOn and water quality assessment (project CUP: B83C24009260005).

## Disclosures

The authors declare no conflicts of interest.

## Data Availability

Data are publicly available at [56]

## References

1. A. Koehler, A. Anderson, A. Andrade, *et al.*, “Sources, fate and effects of microplastics in the marine environment: a global assessment,” *J. Ser. GESAMP Reports Stud.* **90**, 96 (2015).
2. J. Liu, J. Niu, W. Wu, *et al.*, “Recent advances in the detection of microplastics in the aqueous environment by electrochemical sensors: A review,” *Mar. pollution bulletin* **214**, 117695 (2025).
3. S. Thodhal Yoganandham, N. Hamid, M. Junaid, *et al.*, “Micro(nano)plastics in commercial foods: A review of their characterization and potential hazards to human health,” *Environ. Res.* **236**, 116858 (2023).
4. Z. S. Mazhandu, E. Muzenda, T. A. Mamvura, *et al.*, “Integrated and consolidated review of plastic waste management and bio-based biodegradable plastics: Challenges and opportunities,” *Sustainability* **12**, 8360 (2020).
5. J. Boucher and D. Friot, *Primary Microplastics in the Oceans: A Global Evaluation of Sources* (IUCN, Gland, Switzerland, 2017).
6. J. Sun, X. Dai, Q. Wang, *et al.*, “Microplastics in wastewater treatment plants: Detection, occurrence and removal,” *Water Res.* **152**, 21–37 (2019).
7. B. Henry, K. Laitala, and I. G. Klepp, “Microfibres from apparel and home textiles: Prospects for including microplastics in environmental sustainability assessment,” *Sci. The Total. Environ.* **652**, 483–494 (2019).
8. F. De Falco, M. P. Gullo, G. Gentile, *et al.*, “Evaluation of microplastic release caused by textile washing processes of synthetic fabrics,” *Environ. Pollut.* **236**, 916–925 (2018).
9. L. Hildebrandt, N. Voigt, T. Zimmermann, *et al.*, “Evaluation of continuous flow centrifugation as an alternative technique to sample microplastic from water bodies,” *Mar. Environ. Res.* **151**, 104768 (2019).
10. J. Lukose, M. Sunil, E. K. Westhead, *et al.*, “Gaining traction of optical modalities in the detection of microplastics,” *Curr. Opin. Chem. Eng.* **47**, 101086 (2025).
11. Y. Yan, L. Zeng, J. Gao, *et al.*, “Pushing the frontiers of micro/nano-plastic detection with portable instruments,” *TrAC Trends Anal. Chem.* **181**, 118044 (2024).
12. T. Maes, R. Jessop, N. Wellner, *et al.*, “A rapid-screening approach to detect and quantify microplastics based on fluorescent tagging with nile red,” *Sci. Reports* **7**, 44501 (2017).
13. W. J. Shim, S. H. Hong, and S. E. Eo, “Identification methods in microplastic analysis: a review,” *Anal. Methods* **9**, 1384–1391 (2017).
14. C. Zarfl, “Promising techniques and open challenges for microplastic identification and quantification in environmental matrices,” *Anal. Bioanal. Chem.* **411**, 3743–3756 (2019).
15. L. Circelli, Z. Cheng, E. Garwood, *et al.*, “Comparison of atr-ftir and nir spectroscopy for identification of microplastics in biosolids,” *Sci. The Total. Environ.* **916**, 170215 (2024).
16. S. Primpke, C. Lorenz, R. Rascher-Friesenhausen, and G. Gerdts, “An automated approach for microplastics analysis using focal plane array (fpa) ftir microscopy and image analysis,” *Anal. Methods* **9**, 1499–1511 (2017).
17. S. Mintenig, I. Int-Veen, M. Löder, *et al.*, “Identification of microplastic in effluents of waste water treatment plants using focal plane array-based micro-fourier-transform infrared imaging,” *Water Res.* **108**, 365–372 (2017).
18. J. Seghers, E. A. Stefanaki, R. La Spina, *et al.*, “Preparation of a reference material for microplastics in water—evaluation of homogeneity,” *Anal. Bioanal. Chem.* **414**, 385–397 (2021).
19. L. Cabernard, L. Roscher, C. Lorenz, *et al.*, “Comparison of raman and fourier transform infrared spectroscopy for the quantification of microplastics in the aquatic environment,” *Environ. Sci. & Technol.* **52**, 13279–13288 (2018).
20. J. Zhang, K. Tian, C. Lei, and S. Min, “Identification and quantification of microplastics in table sea salts using micro-nir imaging methods,” *Anal. Methods* **10**, 2881–2887 (2018).
21. A. Nayak, E. Malkiel, M. McFarland, *et al.*, “A review of holography in the aquatic sciences: In situ characterization of particles, plankton, and small scale biophysical interactions,” *Front. Mar. Sci.* **7**, 572147 (2021).
22. T. Takahashi, Z. Liu, T. Thevar, *et al.*, “Identification of microplastics in a large water volume by integrated holography and raman spectroscopy,” *Appl. Opt.* **59**, 5073–5078 (2020).
23. V. Bianco, P. Memmolo, P. Carcagni, *et al.*, “Microplastic identification via holographic imaging and machine learning,” *Adv. Intell. Syst.* **2**, 1900153 (2020).
24. V. Bianco, D. Pirone, P. Memmolo, *et al.*, “Identification of microplastics based on the fractal properties of their holographic fingerprint,” *ACS Photonics* **8**, 2148–2157 (2021).
25. I. Sierra, M. Rodriguez, R. Faccio, *et al.*, “Identification of microplastics in wastewater samples by means of polarized light optical microscopy,” *Environ. Sci. Pollut. Res.* **27**, 7409–7419 (2020).
26. J. Li, H. Liu, R. Liao, *et al.*, “Recognition of microplastics suspended in seawater via refractive index by mueller matrix polarimetry,” *Mar. Pollut. Bull.* **188**, 114706 (2023).
27. J. Huang, Y. Zhu, Y. Li, and E. Lam, “Snapshot polarization-sensitive holography for detecting microplastics in turbid water,” *ACS Photonics* **10**, 4483–4493 (2023).

28. M. Valentino, J. Běhal, V. Bianco, *et al.*, “Intelligent polarization-sensitive holographic flow-cytometer: Towards specificity in classifying natural and microplastic fibers,” *Sci. The Total. Environ.* **815**, 152708 (2022).
29. Z. Wang, L. J. Millet, M. U. Gillette, and G. Popescu, “Jones phase microscopy of transparent and anisotropic samples,” *Opt. Lett.* **33**, 1270 (2008).
30. Y. Jiao, M. Kandel, X. Liu, *et al.*, “Real-time jones phase microscopy for studying transparent and birefringent specimens,” *Opt. Express* **28**, 34190–34200 (2020).
31. J. Běhal, M. Valentino, L. Miccio, *et al.*, “Toward an all-optical fingerprint of synthetic and natural microplastic fibers by polarization-sensitive holographic microscopy,” *ACS Photonics* **9**, 694–705 (2022).
32. M. Valentino, J. Běhal, C. Tonetti, *et al.*, “Discernment of textile fibers by polarization-sensitive digital holographic microscope and machine learning,” *Opt. Lasers Eng.* **181**, 108395 (2024).
33. S. Owen, S. Cureton, M. Szuhani, *et al.*, “Microplastic adulteration in homogenized fish and seafood - a mid-infrared and machine learning proof of concept,” *Spectrochimica Acta Part A: Mol. Biomol. Spectrosc.* **260**, 119985 (2021).
34. V. H. da Silva, F. Murphy, J. M. Amigo, *et al.*, “Classification and quantification of microplastics (<100  $\mu$ m) using a focal plane array–fourier transform infrared imaging system and machine learning,” *Anal. Chem.* **92**, 13724–13733 (2020).
35. M. Kedzierski, M. Falcou-Préfol, M. E. Kerros, *et al.*, “A machine learning algorithm for high throughput identification of ftir spectra: Application on microplastics collected in the mediterranean sea,” *Chemosphere* **234**, 242–251 (2019).
36. Z. Ballard, C. Brown, A. Madni, and A. Ozcan, “Machine learning and computation-enabled intelligent sensor design,” *Nat. Mach. Intell.* **3**, 1–10 (2021).
37. S. Yuan, C. Ma, E. Fetaya, *et al.*, “Geometric deep optical sensing,” *Science* **379**, eade1220 (2023).
38. P. Freire, E. Manuylovich, J. Prilepsky, and S. Turitsyn, “Artificial neural networks for photonic applications—from algorithms to implementation: tutorial,” *Adv. Opt. Photonics* **15**, 739–834 (2023).
39. R. Bommasani, D. A. Hudson, E. Adeli, *et al.*, “On the opportunities and risks of foundation models,” *CoRR* **abs/2108.07258** (2021).
40. I. Sarker, “Machine learning: Algorithms, real-world applications and research directions,” *SN Comput. Sci.* **2**, 160 (2021).
41. V. Sheth, U. Tripathi, and A. Sharma, “A comparative analysis of machine learning algorithms for classification purpose,” *Procedia Comput. Sci.* **215**, 422–431 (2022). 4th International Conference on Innovative Data Communication Technology and Application.
42. G. Lewicki and G. Marino, “Approximation by superpositions of a sigmoidal function,” *Appl. Math. Lett.* **17**, 1147–1152 (2004).
43. Z. Lu, H. Pu, F. Wang, *et al.*, “The expressive power of neural networks: A view from the width,” *CoRR* p. 6232–6240 (2017).
44. S. Lee, H. Jeong, S. M. Hong, *et al.*, “Automatic classification of microplastics and natural organic matter mixtures using a deep learning model,” *Water Res.* **246**, 120710 (2023).
45. W. Zhang, W. Feng, Z. Cai, *et al.*, “A deep one-dimensional convolutional neural network for microplastics classification using raman spectroscopy,” *Vib. Spectrosc.* **124**, 103487 (2022).
46. K. He, G. Gkioxari, P. Dollar, and R. Girshick, “Mask r-cnn,” in *2017 IEEE International Conference on Computer Vision (ICCV)*, (IEEE, 2017), p. 2961–2969.
47. P. Akkajit, A. Sukkuea, and B. Thongnonghin, “Comparative analysis of five convolutional neural networks and transfer learning classification approach for microplastics in wastewater treatment plants,” *Ecol. Informatics* **78**, 102328 (2023).
48. X.-L. Han, N.-J. Jiang, T. Hata, *et al.*, “Deep learning based approach for automated characterization of large marine microplastic particles,” *Mar. Environ. Res.* **183**, 105829 (2023).
49. Y. Zhu, C. Hang Yeung, and E. Y. Lam, “Microplastic pollution monitoring with holographic classification and deep learning,” *J. Physics: Photonics* **3**, 024013 (2021).
50. P. Russo and F. Di Ciaccio, “Deep classification of microplastics through image fusion techniques,” *IEEE Access* **12**, 134852–134861 (2024).
51. A. Baroni, V. Chamard, and P. Ferrand, “Extending quantitative phase imaging to polarization-sensitive materials,” *Phys. Rev. Appl.* **13**, 054028 (2020).
52. S.-Y. Lu and R. A. Chipman, “Homogeneous and inhomogeneous jones matrices,” *J. Opt. Soc. Am. A* **11**, 766 (1994).
53. I. Goodfellow, Y. Bengio, and A. Courville, *Deep Learning* (MIT Press, 2016). <http://www.deeplearningbook.org>.
54. N. Srivastava, G. Hinton, A. Krizhevsky, *et al.*, “Dropout: A simple way to prevent neural networks from overfitting,” *J. Mach. Learn. Res.* **15**, 1929–1958 (2014).
55. D. P. Kingma and J. Ba, “Adam: A method for stochastic optimization,” *CoRR* **abs/1412.6980** (2014).
56. J. Appel, “GitHub repository: Microfiber classification,” <https://github.com/JanAppelCZ/microfiber-classification> (2026).
57. H. Peng, F. Long, and C. Ding, “Feature selection based on mutual information criteria of max-dependency, max-relevance, and min-redundancy,” *IEEE Trans. on Pattern Anal. Mach. Intell.* **27**, 1226–1238 (2005).
58. M. Radovic, M. Ghalwash, N. Filipovic, and Z. Obradovic, “Minimum redundancy maximum relevance feature selection approach for temporal gene expression data,” *BMC Bioinform.* **18**, 9 (2017).
59. S. M. Lundberg and S.-I. Lee, “A unified approach to interpreting model predictions,” in *Neural Information Processing Systems*, vol. 20 (2017), pp. 4765–4774.

60. S. M. Lundberg, G. Erion, H. Chen, *et al.*, “From local explanations to global understanding with explainable ai for trees,” *Nat. Mach. Intell.* **2**, 56–67 (2020).
61. A. V. Ponce Bobadilla, V. Schmitt, C. Maier, *et al.*, “Practical guide to shap analysis: Explaining supervised machine learning model predictions in drug development,” *Clin. Transl. Sci.* **17** (2024).
62. C. Frye, D. de Mijolla, T. Begley, *et al.*, “Shapley explainability on the data manifold,” in *International Conference on Learning Representations*, (2021).
63. C. Molnar, G. König, J. Herbinger, *et al.*, “General pitfalls of model-agnostic interpretation methods for machine learning models,” in *xxAI - Beyond Explainable AI: International Workshop, Held in Conjunction with ICML 2020, July 18, 2020, Vienna, Austria, Revised and Extended Papers*, A. Holzinger, R. Goebel, R. Fong, *et al.*, eds. (Springer International Publishing, Cham, 2022), pp. 39–68.
64. A. El-Nemr, ed., *Textiles* (Nova Science, Hauppauge, NY, 2012).
65. I. H. Mondal, ed., *Fundamentals of natural fibres and textiles*, The Textile Institute Book Series (Woodhead Publishing, 2021).
66. A. Haji, R. S. Rahbar, and B. Kalantari, “The effect of hot multistage drawing on molecular structure and optical properties of polyethylene terephthalate fibers,” *Mater. Res.* **15**, 554–560 (2012).
67. R. Huijts and S. Peters, “The relation between molecular orientation and birefringence in pet and pen fibres,” *Polymer* **35**, 3119–3121 (1994).
68. Y. Okada, O. Urakawa, and T. Inoue, “Reliability of intrinsic birefringence estimated via the modified stress-optical rule,” *Polym. J.* **48**, 1073–1078 (2016).
69. J. Lekner, “Reflection and refraction by uniaxial crystals,” *J. Phys. Condens. Matter* **3**, 6121–6133 (1991).